

# The small and the beautiful: How the star formation law affects galactic disk structure

H. Braun<sup>1\*</sup> and W. Schmidt<sup>1,2†</sup>

<sup>1</sup>*Institut für Astrophysik, Universität Göttingen, Friedrich-Hund Platz 1, D-37077 Göttingen, Germany*

<sup>2</sup>*Hamburger Sternwarte, Universität Hamburg, Gojenbergsweg 112, D-21029 Hamburg, Germany*

Draft version, July 2015

## ABSTRACT

We investigate the influence of different analytical parameterizations and fit functions for the local star formation rate in AMR simulations of an isolated disk galaxy with the Nyx code. Such parameterizations express the star formation efficiency as function of the local turbulent Mach number and viral parameter. By employing the method of adaptively refined large eddy simulations, we are able to evaluate these physical parameters from the numerically unresolved turbulent energy associated with the grid scale. We consider both single and multi free-fall variants of star formation laws proposed by Padoan & Nordlund, Hennebelle & Chabrier, and Krumholz & McKee. We find that the global star formation rate and the relation between the local star formation rate and the gas column density is reproduced in agreement with observational constraints by all multi free-fall models of star formation. Some models with obsolete calibration or a single free-fall time scale, however, result in an overly clumpy disk that does not even remotely resemble the structure of observed spirals.

**Key words:** methods: numerical - galaxies: ISM - stars: formation - turbulence

## 1 INTRODUCTION

Numerical simulations of disk galaxies cannot fully resolve processes in the interstellar medium (ISM) such as star formation and feedback from supernova (SN) explosions. For this reason, effective models for these processes are used in large-scale simulations, which are called sub-resolution or sub-grid scale (SGS) models. The most commonly applied model of star formation is based on the empirical Kennicutt-Schmidt (KS) relation (e.g. Schmidt 1959; Kennicutt 1998; Gao & Solomon 2004; Daddi et al. 2010; Genzel et al. 2010; Lada et al. 2010; Bigiel et al. 2011; Kennicutt & Evans 2012; Schruba 2013; Roychowdhury et al. 2015). Formulated as an SGS model, this relation translates to

$$\dot{\rho}_s = \epsilon_{\text{ff}} \frac{\rho}{\tau_{\text{ff}}}, \quad (1)$$

where  $\rho$  can be either the total gas density (e.g. Renaud et al. 2013; Agertz et al. 2013; Lagos et al. 2015; Tasker et al. 2015) or some fraction of that density (for example, the molecular hydrogen density as in Gnedin et al. (2009), Dobbs & Pringle (2013), or Agertz & Kravtsov (2014)),  $\tau_{\text{ff}} \sim (G\rho)^{-1/2}$  is the free-fall time scale associated with  $\rho$ , and  $\epsilon_{\text{ff}}$  the so-called star formation efficiency. The coefficient  $\epsilon_{\text{ff}}$  is usually assumed to be a constant, i. e. a freely tunable numerical pa-

rameter, in disk galaxy simulations. This constant is chosen such that the global star formation rate matches observational values. However, numerical studies and observations of star-forming regions in galaxies suggest significant local variations of the star formation efficiency (Evans et al. 2009; Onodera et al. 2010; Murray 2011).

Also from the theoretical point of view, the star formation efficiency should change with the local conditions in the ISM because stars form from gravitationally unstable density enhancements seeded by turbulence in molecular clouds (e.g. Mac Low & Klessen 2004; McKee & Ostriker 2007; Hennebelle & Falgarone 2012). Although the dynamics of star-forming clouds appears to be extremely complex (compressible turbulence, self-gravity, magnetic fields, radiative cooling and heating), attempts have been made to capture the essence of the star formation process in relatively simple analytical relationships between the star formation rate or efficiency and some fundamental parameters. In particular, star formation efficiencies were parameterized in terms of the turbulent Mach number (corresponding to the ratio of turbulent and thermal energies) and the viral parameter (the ratio of turbulent and gravitational energies). An representative example is the relation proposed by Padoan & Nordlund (2011) (a complete overview will be given in Section 2), which is based on the idea that the typical length scale of dense clumps is given by the thickness of shock layers for a particular Mach number of turbulence and that the

\* E-mail: hbraun@astro.physik.uni-goettingen.de

† E-mail: wolfram.schmidt@uni-hamburg.de

clumps become unstable if they exceed their Jeans mass (this is where the viral parameter comes in). The distribution of density enhancements is determined by a log-normal density distribution, which again depends on the turbulent Mach number. Braun et al. (2014) [hereafter BS14] exploited this relation in order to dynamically compute the efficiency parameter in simulations of an isolated disk galaxy, rather than assuming some specific value. It turned out that this kind of SGS model is able to predict typical star formation efficiencies in galaxies (e.g. Gao & Solomon 2004; Daddi et al. 2010; Genzel et al. 2010; Murray 2011) without making use of the observed relations for the star formation rate as input. However, an open question is whether the properties of simulated disk galaxies are sensitive to the various assumptions that go into the star formation model. If that were the case, it should be easily possible to discriminate existing models, which make entirely different basic assumptions. On the other hand, it is also possible that different models produced comparable effects under conditions that favour star formation.

Another essential component of a SGS model for realistic galaxy simulations is stellar feedback. There is a great variety of different approaches and extensive studies of the influence of feedback models on the properties of simulated galaxies (e.g. Stinson et al. 2006, 2013; Wise et al. 2012; Agertz et al. 2013; Hopkins et al. 2014). Here we focus on the influence of the star formation model on global properties of simulated isolated disk galaxies for one particular feedback model, namely the mixed thermal and turbulent feedback introduced in BS14. It was demonstrated that this model produces reasonable results and therefore can be considered as a reliable reference point for further studies.

This article is structured as follows. After outlining the applied numerical methods and summarising the star formation models implemented in our code (Section 2), we present the results from our simulations in Section 3. In particular, we consider the global star formation rate, the structure of the gaseous disk, the relations between the local star formation rate and surface densities, and the role of turbulence for the different models. The results of our study are summarised and discussed in Section 4.

## 2 NUMERICAL METHODS AND MODELS

The simulations presented in this study were carried out using the cosmological hydrodynamics code *Nyx* (Almgren et al. 2013). *Nyx* solves the Euler equations on an adaptively refined grid using the piecewise parabolic method. Collisionless components like stellar particles are taken into account as N-body system via a particle-mesh approach. In our simulations, we included the SGS model introduced by Schmidt & Federrath (2011) and Schmidt et al. (2014) to model turbulent motions below the resolution scale. Non-adiabatic sub-resolution processes are modelled using the MIST (Multi-phase Interstellar medium with Star formation and Turbulence) model, which was proposed in Braun & Schmidt (2012) and BS14. The employed physics encompasses:

- *Self gravity* from gas and stars.
- *Gas dynamics* using piecewise parabolic method for the

resolved motions and the SGS model for unresolved turbulence.

- *Radiative cooling* from gas, metals, and dust.
- *Multi-phase ISM* consisting of a diffuse warm, a clumpy cold, and a hot phase for SN ejecta.
- *Star formation rate* depending on the locally inferred molecular fraction and the thermal and turbulent state of the gas.
- *Stellar feedback* in the form of a combination of thermal and turbulent feedback from SN and thermal feedback from Lyman continuum heating, both depending on the age of the stars.
- *Metal enrichment* due to SN.

As demonstrated in BS14, simulations featuring MIST in combination with a SGS turbulence model are able to simultaneously reproduce several observed properties of star formation in a plausible way. Owing to the combined effect of turbulent plus thermal SN-feedback and a non-cooling, but decaying hot gas-phase of SN-ejecta the so-called overcooling problem is avoided. The star formation relations of KS-type following from the simulation data are a genuine result of the modelling, as they were not a priori imposed in the model. Moreover, MIST allows us to probe the behaviour of different theoretical approaches to the calculation of the star formation rate in the cold molecular gas by incorporating the corresponding parameterizations in our simulations.

### 2.1 Multi-phase and star formation models

MIST separates the gas content of a numerical resolution element into two fractions – or phases: a clumpy cold phase and a diffuse warm phase, within which the cold clumps are embedded. The fractional densities of the cold and warm phases are determined by partial differential equations with source terms related to various exchange processes between the phases and star formation, which converts cold gas into stellar mass (see Figures 1 and 2 of BS12 for an overview). While the warm phase is subject to radiative cooling and feeds the clumpy cold phase through this channel, the cold phase itself is kept at a constant temperature of  $T_c = 50$  K. The heating of cold gas is modelled as mass transfer into the warm phase, which has a variable temperature following from the hydrodynamical energy equation. Under adiabatic conditions, the total energy of the two phases is conserved. Moreover, shielded molecular gas may reside inside the cold clumps. The mass fraction  $f_{\text{H}_2}$  of molecular gas is estimated using a Strömberg-like approach.

Only this molecular fraction  $f_{\text{H}_2}\rho_c$  of the cold gas with fractional density  $\rho_c$  is allowed to form stars at a rate  $\dot{\rho}_s$  given by

$$\dot{\rho}_s = \frac{\epsilon_{\text{core}}\epsilon_{\text{mod}}f_{\text{H}_2}\rho_c}{\tau_{c,\text{ff}}}. \quad (2)$$

$\tau_{c,\text{ff}}$  is the free-fall time scale within the cold clumps

$$\tau_{c,\text{ff}} = \sqrt{\frac{3\pi}{32G\rho_{c,\text{pa}}}}, \quad (3)$$

with the gravitational constant  $G$  and the average density inside the cold phase  $\rho_{c,\text{pa}}$ , which differs from the fractional density  $\rho_c$ . To calculate the average densities, an equilibrium between the effective (thermal plus turbulent) pressures of

the cold and warm phases is assumed at the typical clump scale  $\ell_c$  (for a thorough description see BS12; BS14). The coefficient  $\epsilon_{\text{mod}}$  in equation (2) specifies the efficiency of forming gravitationally bound cores with respect to the free-fall time scale  $\tau_{c,\text{ff}}$ .  $\epsilon_{\text{core}}$  is the mass fraction of the bound cores that eventually ends up in stars, while the rest is ejected in the prestellar phase. No explicit density threshold is imposed on the total gas density  $\rho$  or the the average density of cold phase,  $\rho_{c,\text{pa}}$ . The only requirement for star formation is the existence of shielded molecular gas inside the cold clumps, which depends on  $\rho_{c,\text{pa}}$ ,  $\ell_c$ , and the metallicity  $Z$ .

A unique feature of MIST is that  $\epsilon_{\text{mod}}$  is not assumed to be a constant coefficient, but is treated as a variable of the model, which is computed from the current local state of the gas in the cold clumps. This is achieved by modelling the substructure of the ISM and turbulence below the resolution scale on the basis of the numerically unresolved turbulent energy  $K_{\text{SGS}}$ , which determines key parameters in the expressions for  $\epsilon_{\text{mod}}$  following from analytical theories of star formation.

In BS12 and BS14, the model of Padoan & Nordlund (2011, hereafter PN11) in the parameterization of Federrath & Klessen (2012, in the following FK12) were used. In this study, we explore the effects of different choices for  $\epsilon_{\text{mod}}$  based on the analytical models proposed by PN11, Krumholz & McKee (2005, hereafter KM05), and Hennebelle & Chabrier (2008, 2009, 2011, 2013, hereafter HC08-13). While these models result from theoretical reasoning, a simple star formation law was put forward by Padoan et al. (2012, hereafter PHN12) by fitting data from simulations of driven isothermal turbulence in self-gravitating gas.

In the context of the analytical models,  $\epsilon_{\text{mod}}$  can be understood as an  $x$ -weighted integral of the probability density function  $\text{pdf}(x)$  over the logarithmic overdensity ratio  $x = \log(\tilde{\rho}/\rho_{c,\text{pa}})$  above a certain critical threshold  $x_{\text{cr}} = \log(\tilde{\rho}_{\text{cr}}/\rho_{c,\text{pa}})$ , which separates gravitationally bound from unbound structures in the turbulent gas. To account for a collapse time scale that varies with the density fluctuation  $x$ , multi free-fall (mff) models incorporate the weighing factor  $f_{\text{ff}} = \tau_{c,\text{ff}}/\tau_{\text{ff}}(\tilde{\rho}) = \exp^{1/2}(x)$  into the integral. In general,  $\epsilon_{\text{mod}}$  can be written as

$$\epsilon_{\text{mod}} = f_{\text{cal}} \int_{x_{\text{cr}}}^{\infty} f_{\text{ff}}(x) \exp(x) \text{pdf}(x) dx. \quad (4)$$

The arbitrary prefactor  $f_{\text{cal}}$  ( $1/\phi_t$  in FK12) has to be calibrated by fitting the star formation efficiency to numerical data from simulations of self-gravitating turbulence.

Although  $\text{pdf}(x)$  tends to develop a power-law tail in strongly self-gravitating gas, the analytical models generally assume a log-normal shaped PDF, which is characteristic for supersonic isothermal turbulence:

$$\text{pdf}(x) = \frac{1}{\sqrt{2\pi\sigma_x^2}} \exp\left(-\frac{(x-x_0)^2}{2\sigma_x^2}\right), \quad (5)$$

where

$$\sigma_x^2 = \log(1 + b^2 \mathcal{M}^2), \quad (6)$$

determines the width of the distribution and  $x_0 = -\sigma_x^2/2$  is

the logarithmic mean. Apart from the compressive factor<sup>1</sup>

$$b = \begin{cases} 1 & \text{if local SNe feedback is active} \\ 0.5 & \text{in quiescent regions} \end{cases}, \quad (7)$$

which was introduced by Federrath et al. (2010),  $\sigma_x$  depends on the root-mean-square Mach number  $\mathcal{M}$  of turbulent motions in the cold clumps. We estimate  $\mathcal{M}$  in our simulations by extrapolating the turbulent SGS energy from the grid scale to the clump scale  $\ell_c$  by assuming a power law for the scale dependence of turbulent velocity fluctuations:

$$\mathcal{M} = \sqrt{\frac{2K_{\text{SGS}}(\ell_c/\Delta)^{2\eta_w}}{\gamma(\gamma-1)e_c}} \quad (8)$$

with the specific thermal energy of the cold phase  $e_c = e(T_c = 50 \text{ K})$ , the polytropic index of the equation of state of the gas  $\gamma = 5/3$ , the specific kinetic energy  $K_{\text{SGS}}$  of motions below resolution scale  $\Delta$ , and the turbulent velocity scaling exponent  $\eta_w = 1/3$ .

Basically, the differences between the analytical models amount to different definitions of  $x_{\text{cr}}$  and  $f_{\text{ff}}$ . The critical overdensity  $x_{\text{cr}}$  is in all cases a function of  $\mathcal{M}$  and the virial parameter  $\alpha_{\text{vir}}$  of the cold clumps, where

$$\alpha_{\text{vir}} = \frac{10K_{\text{SGS}}(\ell_c/\Delta)^{2\eta}}{\pi G \ell_c^2 \rho_{c,\text{pa}}}. \quad (9)$$

In addition to the models in their originally published form, we also consider the single and multi free-fall formulations with the best-fit calibrations as provided by FK12 in their tables 1 and 3. A comprehensive list of all the models used in this study is given in Table 1. The main ideas behind these models are briefly summarised in the following. For a more detailed account see FK12 and the original papers.<sup>2</sup>

### 2.1.1 PN family

PN11 assume that the size of a critical Bonnor-Ebert-sphere is equal to the typical thickness of a shocked layer, which is computed from the combination of the isothermal shock jump conditions and a turbulent velocity scaling relation  $u'(\ell) \propto \ell^{\eta_c}$  with  $\eta_c = 0.5$ . This implies

$$\exp(x_{\text{cr}}) = 0.0067 \theta^{-2} \alpha_{\text{vir}} \mathcal{M}^2. \quad (10)$$

In the MIST framework,  $\theta \ell_c$  is the injection scale of supersonic turbulence in a cloud. In the case of our fiducial model PN-FK we simply set  $\theta = 1.0$ , while  $\theta = 0.35$  in PN11 and  $\theta = 0.65$  in table 3 of FK12). We chose the intermediate value  $\theta = 0.5$  for our PN run to explore the influence of this coefficient. Both the original PN11 model and PN-FK assume a constant free-fall time factor  $f_{\text{ff}} = \exp^{1/2}(x_{\text{cr}})$ , i.e.

<sup>1</sup> This definition assumes that turbulence injection driven due to SNe is dominated by compressive/dilatational forces. Otherwise a mixture of compressive and solenoidal driving forces resulting from shearing motions in the galactic disk, local gravitational collapse, or motions triggered by thermal instabilities of the multi-phase ISM is assumed.

<sup>2</sup> In the following we refer to different subsets out of our simulation suite as families. PN, PN-FK, and PN-FK-mff belong to the PN-family, HC, HC-FK, and HC-FK-mff to the HC-family, and KM, KM-FK, and KM-FK-mff accordingly to the KM-family.

**Table 1.** Overview of star formation models implemented into MIST. For a brief description of the models and definitions of the various coefficients and parameters, see Sections 2.1.1–2.1.3.

ID	critical overdensity ratio $\exp(x_{\text{cr}})$	ff-time factor $f_{\text{ff}}$	SF efficiency $\epsilon_{\text{mod}}$	coefficients	references
models and coefficients as in original publication (see listed reference – if they did not suggest a value, we chose $f_{\text{cal}} = 1$ )					
PN	$(0.0067)\theta^{-2}\alpha_{\text{vir}}\mathcal{M}^2$	$\exp^{1/2}(x_{\text{cr}})$	$f_{\text{cal}} \times a_2$	$\theta = 0.5, f_{\text{cal}} = 1.0$	PN11
HC	$(\pi^2/5)y_{\text{cut}}^{-1}\alpha_{\text{vir}}\left(y_{\text{cut}}^{-1}\mathcal{M}^{-2} + 1/3\right)$	$\exp^{1/2}(x)$	$f_{\text{cal}} \times a_3$	$y_{\text{cut}} = 0.1, f_{\text{cal}} = 1.0$	HC08-13
KM	$(\pi^2/5)\phi_x^2\alpha_{\text{vir}}\mathcal{M}^2$	1	$f_{\text{cal}} \times a_1$	$\phi_x = 1.12, f_{\text{cal}} = 1.92$	KM05
PHN	n.a.	n.a.	$\exp[\varphi\pi^2\alpha_{\text{vir}}]$	$\varphi = -0.003$	PHN12
calibrated by FK12 (see their table 1 for analytic forms and their table 3 (HD-fit) for the coefficients)					
PN-FK	$(0.0067)\theta^{-2}\alpha_{\text{vir}}\mathcal{M}^2$	$\exp^{1/2}(x_{\text{cr}})$	$f_{\text{cal}} \times a_2$	$\theta = 1.0, f_{\text{cal}} = 1.5$	PN11; FK12
HC-FK	$(\pi^2/5)y_{\text{cut}}^{-1}\alpha_{\text{vir}}\left(y_{\text{cut}}^{-1}\mathcal{M}^{-2} + 1/3\right)$	$\exp^{1/2}(x)$	$f_{\text{cal}} \times a_3$	$y_{\text{cut}} = 1.3, f_{\text{cal}} = 0.24$	HC08-13; FK12
KM-FK	$(\pi^2/5)\phi_x^2\alpha_{\text{vir}}\mathcal{M}^2$	1	$f_{\text{cal}} \times a_1$	$\phi_x = 0.12, f_{\text{cal}} = 3.0$	KM05; FK12
multi free-fall (mff), calibrated by FK12 (see their table 1 for analytic forms and table 3 (HD-fit) for the coefficients)					
PN-FK-mff	$(0.0067)\theta^{-2}\alpha_{\text{vir}}\mathcal{M}^2$	$\exp^{1/2}(x)$	$f_{\text{cal}} \times a_3$	$\theta = 1.0, f_{\text{cal}} = 0.49$	PN11; FK12
HC-FK-mff	$(\pi^2/5)y_{\text{cut}}^{-2}\alpha_{\text{vir}}\mathcal{M}^{-2}$	$\exp^{1/2}(x)$	$f_{\text{cal}} \times a_3$	$y_{\text{cut}} = 1.1, f_{\text{cal}} = 0.21$	HC08-13; FK12
KM-FK-mff	$(\pi^2/5)\phi_x^2\alpha_{\text{vir}}\mathcal{M}^2$	$\exp^{1/2}(x)$	$f_{\text{cal}} \times a_3$	$\phi_x = 0.19, f_{\text{cal}} = 0.49$	KM05; FK12

**Definitions:**

$$\begin{aligned}
a_1 &= 0.5 \left(1 + \operatorname{erf}\left[\frac{(\sigma_x^2 - 2x_{\text{cr}})/(8\sigma_x^2)^{1/2}}{1}\right]\right); \\
a_2 &= 0.5 \left(1 + \operatorname{erf}\left[\frac{(\sigma_x^2 - 2x_{\text{cr}})/(8\sigma_x^2)^{1/2}}{1}\right]\right) \exp(x_{\text{cr}}/2); \\
a_3 &= 0.5 \left(1 + \operatorname{erf}\left[\frac{(\sigma_x^2 - x_{\text{cr}})/(2\sigma_x^2)^{1/2}}{1}\right]\right) \exp(3\sigma_x^2/8)
\end{aligned}$$

the effective free-fall time scale is given by the critical overdensity  $\tilde{\rho}_{\text{cr}}$  rather than the mean density  $\rho_{\text{c,pa}}$  of the cold phase.

*2.1.2 HC family*

The model suggested by HC08-13 is based on the assumption that bound substructures of a turbulent gas cloud collapse on time scales determined by the mean densities of the substructures rather than the whole cloud. The star formation efficiency is then obtained by integrating the mass spectrum of substructures weighted by their free-fall time factors. This integral is truncated at a certain mass fraction  $y_{\text{cut}}$  to avoid overly large structures. While HC08-13 suggested  $y_{\text{cut}} \approx 0.1$ , FK12 concluded from their fits to simulation data that  $y_{\text{cut}}$  slightly above unity is favoured. This would imply that about the whole cloud could collapse, which is unlikely for real star-forming clouds.

Assuming that additional non-thermal support against gravity must increase the stability range (a notion that was questioned by Schmidt et al. 2013), the critical overdensity is defined by requiring that the turbulent Jeans length  $\lambda_{\text{J,t}}(\rho_{\text{cr}})$

$$\lambda_{\text{J,t}}(\rho_{\text{cr}}) = \sqrt{\frac{\pi\gamma(\gamma-1)e_{\text{c}} + 2\pi\lambda_{\text{J,t}}(\rho_{\text{cr}})K_{\text{SGS}}\left(\frac{\ell_{\text{c}}}{\Delta}\right)^{2\eta_{\text{w}}}}{G\rho_{\text{cr}}}} \quad (11)$$

equals the size  $y_{\text{cut}}\ell_{\text{c}}$  of the largest collapsing substructures. This condition leads to a quadratic equation in  $\ell_{\text{c}}$ . Substituting the definitions of  $\mathcal{M}$  and  $\alpha_{\text{vir}}$  yields

$$\exp(x_{\text{cr}}) = \frac{\pi^2\alpha_{\text{vir}}}{5y_{\text{cut}}^2\mathcal{M}^2} + \frac{\pi^2\alpha_{\text{vir}}}{15y_{\text{cut}}}. \quad (12)$$

This expression is used for the models HC and HC-FK. Following FK12, the second term is dropped for the HC-FK-mff

model. For the HC family, 'mff' is actually a misnomer because all models in this family feature the multi free-fall time factor  $f_{\text{ff}} = \exp^{-1/2}(x)$ .

*2.1.3 KM family*

KM05 argue that the critical overdensity follows from the condition that the sonic length is close to the Jeans length. From this condition it follows that

$$\exp(x_{\text{cr}}) = (\pi^2/5)\phi_x^2\alpha_{\text{vir}}\mathcal{M}^2. \quad (13)$$

Apart from the prefactor, the resulting expression for  $\exp(x_{\text{cr}})$  is the same as for the models in the PN family. The fudge factor  $\phi_x$  should be of the order unity. KM05 obtain the best fit for  $\phi_x = 1.12$ . However, FK12 determined smaller values ( $\phi_x \sim 0.1 \dots 0.2$ ).

The main difference between the original PN and KM models is that there is no free-fall time factor at all in the KM models ( $f_{\text{ff}} = 1$  in the case of KM and KM-FK). This means that KM05 assume that the free-fall time scale is just given by the mean density of the cold gas (see equation 3 for  $\tau_{\text{c,ff}}$ ), while PN and PN-FK set the effective free-fall time scale in the star formation law equal to  $\tau_{\text{ff}}(\tilde{\rho}_{\text{cr}})$  (in this case,  $\tau_{\text{c,ff}}$  cancels out from equation 2 for the star formation rate). The mff variants of the KM and PN models, on the other hand, are formally the same.

**2.2 Simulations**

For each of the ten star formation models in Table 1 a simulation run of an idealised isolated disk galaxy was performed with *Nyx* (Almgren et al. 2013) using the methodology from (BS14). As initial condition we used data obtained from the

'ref' run with the fiducial PN-FK model in (BS14) at a simulated age of roughly 1 Gyr. Starting the simulations for our comparison from a pre-evolved galaxy has several benefits. Employing an aged galaxy as initial condition minimises transient effects of the rapid initial growth of the stellar mass and the metallicity within the galactic disk. Since we begin with a statistically stationary star forming configuration of the galactic disk, in which star formation and stellar feedback effects are nearly balanced, it is easy to detect the changes of the disk configuration after switching to a different star formation model.

The 'ref' run of BS14 simulated the evolution of an idealised isolated disk galaxy residing in a box of  $(0.5 \text{ Mpc})^3$  size with the PN-FK model. With a root grid of  $256^3$  and 6 levels of adaptive mesh refinement an effective resolution of 30 pc was achieved. The galaxy in 'ref' was initialised as an adiabatically stable, rotating gas disk of  $10^{10} M_{\odot}$  mass using the potential-method described by Wang et al. (2010). The static potential of an NFW-shaped dark matter halo of  $10^{12} M_{\odot}$  is added to the self-gravity of the gaseous disk. There was no initial stellar component. Radiative cooling causes the initially thick and hot disk to rapidly collapse into a fragmenting thin disk.

After 1 Gyr of evolution, about 30 per cent of the initial total gas mass has been converted into stars. While the majority of the long-lived stars are rather smoothly distributed over the inner disk, many young stars reside in stellar clusters with a typical lifetime of a few 100 Myr. The gas content of the inner, star forming part of the disk is below 50 per cent. At this stage, the simulated galaxy roughly resembles a disk galaxy in a quiescent star forming state with a global star formation rate of  $\sim 1 M_{\odot} \text{ yr}^{-1}$  governed by the self-regulation between star formation and stellar feedback.<sup>3</sup> We use this configuration as initial condition for our comparison runs by following the disk evolution over additional 0.4 Gyr with different star formation models. The time period of 0.4 Gyr corresponds to one orbital revolution at 10 kpc distance from the galactic centre or roughly ten times the maximum age of a stellar particle producing feedback due to SNe of type II.

### 3 RESULTS

#### 3.1 Global star formation rate

The star formation rate integrated over the whole disk is plotted as function of time in Fig. 1 for all runs. After a short transitional phase, in which the disk configuration adjusts itself to the new conditions set by the star formation model, the global star formation rate  $\dot{M}_{\text{SF}}$  settles on average between  $2 \dots 3 M_{\odot} \text{ yr}^{-1}$  in the majority of the runs (PN-family, HC-family, and KM-FK-mff). In the bottom panel of Fig. 1, short term variations are smoothed out by applying a moving average with width of  $\sim 80$  Myr. These variations, which can be as large as  $1 M_{\odot} \text{ yr}^{-1}$  in amplitude, are a consequence of the life-cycle of individual star forming regions in

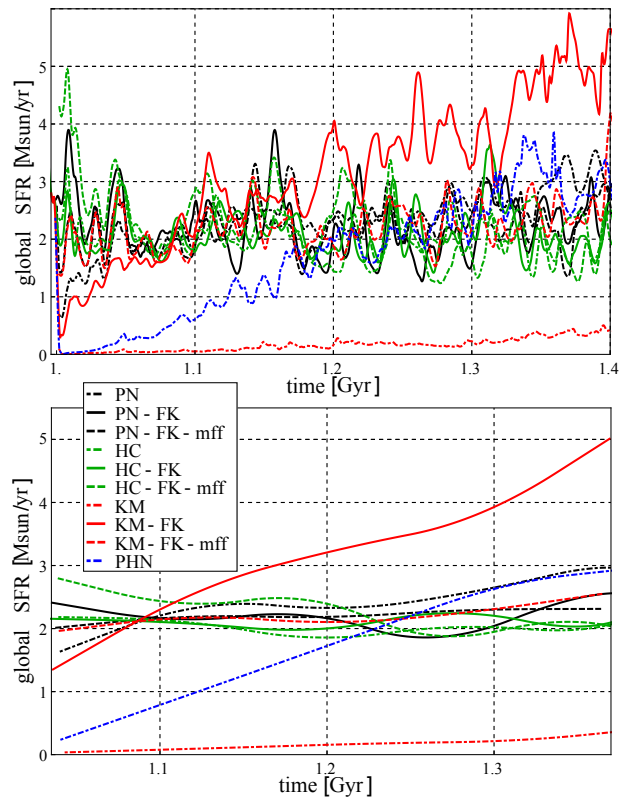


**Figure 1. Top panel:** Global star formation rate  $\dot{M}_{\text{SF}}$  versus simulation time for runs using the different star formation models listed in Table 1. The evolution of  $\dot{M}_{\text{SF}}$  in runs with PN11-family models is drawn in black, with HC08-13-family models in green, with KM05-family models in red, and with the PHN12 model in blue. A model in its original version is indicated by a dot-dashed line, its FK12-calibrated version by a solid line, and its FK12-calibrated multi free-fall version by a dashed line. **Bottom panel:** Same as above, but  $\dot{M}_{\text{SF}}$  is smoothed on a time scale of 80 Myr using a moving average to filter out short term variations.

the disks. As explained in BS14, the associated time scale of about  $10 \dots 30$  Myr arises from delayed SNe feedback. This time scale is consistent with observational estimates of the life-time of star forming gas clouds (e.g. Blitz et al. 2007; McKee & Ostriker 2007; Miura et al. 2012) and is also reproduced by numerical simulations (e.g. Hopkins et al. 2012; Tasker et al. 2015; Dobbs & Pringle 2013). The smoothed time evolution of  $\dot{M}_{\text{SF}}$  is similar for most runs, including the PN-FK run, which merely continues the 'ref' run of BS14.

However, the runs KM, KM-FK, and PHN exhibit deviating behaviour. These three runs have in common that  $\dot{M}_{\text{SF}}$  drops well below  $1 M_{\odot} \text{ yr}^{-1}$  shortly after the start of the simulation and then gradually grows until the simulation is stopped. Only the PHN run with the simple star formation model seems to enter a self-regulated regime toward the end of the simulation, where  $\dot{M}_{\text{SF}}$  approaches a similar level as in the other simulations. While the KM-FK model leads to an overproduction of stars compared to the continuation of the 'ref' run with the PN-FK model, the original KM model falls much below the expected star formation rate. The deviations observed for the KM approach are remedied with the multi free-fall modification of the star formation law. Otherwise, the global star formation rate appears to

<sup>3</sup> Our configuration is not comparable to a star-burst galaxy at high redshift such as the 'HighZ' runs in Hopkins et al. (2011). After 1 Gyr, the conditions in the inner disk of our simulation roughly correspond to the 'Sbc' runs in that paper.

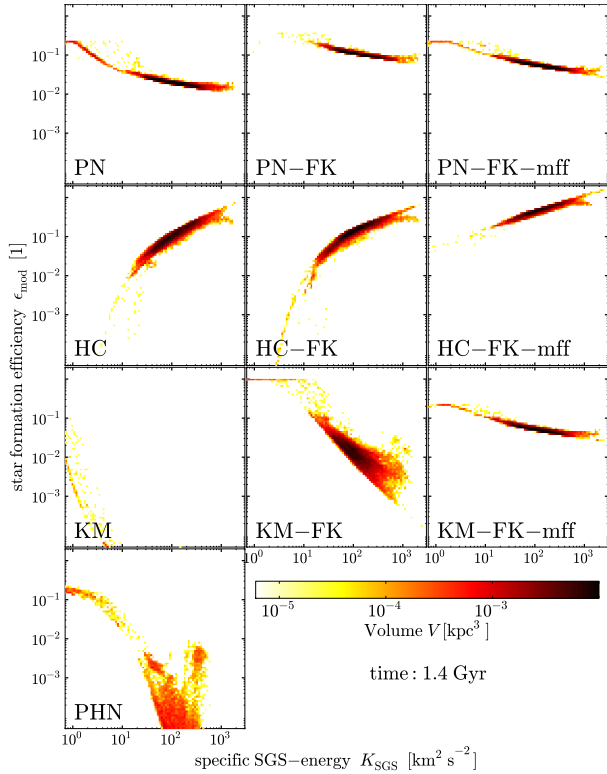


**Figure 2.** Comparison of area-weighted 2D histograms of the star formation efficiency  $\epsilon_{\text{mod}}$  in the cold phase vs. the SGS turbulence energy  $K_{\text{SGS}}$  at an age of  $\sim 1.4$  Gyr. The area is logarithmically colour-coded.

be quite robust with respect to the parameterization of star formation.

### 3.2 Turbulence

Star formation occurs for all included models preferentially around the sweet spot at specific SGS energies of  $K_{\text{SGS}} \sim 100 \text{ km}^2 \text{ s}^{-1}$ . This corresponds to a preferred velocity dispersion of  $\sigma_{\mathbf{u}} \sim 10 \text{ km s}^{-1}$  on the grid resolution scale  $\Delta \approx 30 \text{ pc}$ , implying turbulent Mach numbers around 10 in the cold clouds on the length scale  $\ell_c$ .<sup>4</sup>

These values are comparable to observational findings (e.g. Leroy et al. 2008; Shetty et al. 2012; Stilp et al. 2013). The intensity of small-scale turbulence in actively star forming regions is mainly determined by stellar feedback, the exchange of mass between warm and cold phases, and the assumed effective pressure balance. Figure 2 shows that the models in the PN- and HC-families as well as the KM-FK-mff model predict roughly comparable star formation efficiencies  $\epsilon_{\text{mod}} \sim 0.1$  (corresponding to star formation time scales of  $\lesssim 100 \text{ Myr}$ ) for the relevant SGS energies around  $100 \text{ km}^2 \text{ s}^{-2}$ , although their dependence on  $K_{\text{SGS}}$  is quite different. The highest efficiencies are obtained for the HC-FK-mff model, while PN tends to produce relatively low efficiencies. This is also reflected by the  $\Sigma_{\text{SF}}\text{-}\Sigma_{\text{H}_2}$ -relations

<sup>4</sup> Note that  $\mathcal{M}_c$  is different from the Mach number  $\sigma_{\mathbf{u}}/c_c$  scaled down from  $\Delta$  to  $\ell_c$  because the latter encompasses both the warm and cold phase.

discussed in section 3.4. Moreover, one can clearly see that the efficiencies following from the KM, KM-FK, and PHN models are far below the plausible range of values in turbulent star-forming regions. For these models, star formation exclusively occurs in regions of exceptionally high density, where efficiencies that are systematically too low are compensated by much shorter free-fall time scales.

The star formation efficiencies obtained with the different models can be understood as follows:

#### 3.2.1 PN family

All PN-family models produce a similar  $\epsilon_{\text{mod}}\text{-}K_{\text{SGS}}$  relation. However, the efficiencies are systematically lower for the original PN model and the implied star formation time scale is about 0.75 Gyr, much longer than  $\sim 100 \text{ Myr}$  for PN-FK and PN-FK-mff. Due to the lower level of  $\epsilon_{\text{mod}}$ , the disk tends to be clumpier. This is mainly a consequence of the chosen model coefficient  $\theta = 0.5$  compared to  $\theta = 1$  for the FK-calibrated variants of the PN-family (see Table 1). This behaviour supports our assumption that  $\ell_c$  should be close to the integral scale of turbulence in cold gas clouds, but the strong sensitivity on the parameter  $\theta$  makes PN-type models difficult to control.

The declining trend of  $\epsilon_{\text{mod}}$  with increasing SGS turbulence energy is due to  $\exp(x_{\text{cr}}) \propto \mathcal{M}^2 \propto K_{\text{SGS}}$  (see equation 10), i.e. stronger turbulence tends to produce thinner shock layers, requiring higher densities to reach the critical mass. This effect is alleviated, however, by the implicit dependence of  $\rho_{c,\text{pa}}$  (the mean density of the cold phase) on  $\mathcal{M}$ . This dependence is a consequence of the effective pressure equilibrium between the phases. Since mostly logarithmic density fluctuations  $x$  close to  $x_{\text{cr}}$  contribute to the integral over the exponential tail of pdf( $x$ ) for  $x > x_{\text{cr}}$ , the weighing factor  $f_{\text{ff}}$  (i.e. single vs. multi free-fall) has only a minor impact.

#### 3.2.2 HC family

All HC-family models are actually multi free-fall models and yield realistic  $\epsilon_{\text{mod}} \sim 0.1$ . As a consequence, the resulting star formation rate is comparable to the PN-FK case, although the trend of  $\epsilon_{\text{mod}}$  with  $K_{\text{SGS}}$  is opposite to the PN family because  $\exp(x_{\text{cr}}) \propto \mathcal{M}^{-2}$  (cf. equation 12 and 10). Omitting the second term in the expression for  $x_{\text{cr}}$  in the case of HC-FK-mff (see Table 1) significantly affects  $\epsilon_{\text{mod}}$  only for values of  $K_{\text{SGS}}$  that are generally lower than in star forming regions.

Although the values chosen for the cutoff mass  $y_{\text{cut}}$  differ by a factor 10 in the HC and HC-FK runs, we do not see a significant impact on  $\epsilon_{\text{mod}}$ . However, this does not necessarily imply that  $y_{\text{cut}}$  is unimportant. Probably the influence of  $y_{\text{cut}}$  is compensated by the calibration factor  $f_{\text{cal}} \approx 0.2$  in the case of HC-FK compared to  $f_{\text{cal}} = 1$  for HC. It is therefore likely that a careful calibration is also required for HC-type models.

#### 3.2.3 KM family

KM-FK-mff differs from PN-FK-mff only by a constant coefficient, which explains the striking similarity of top right

and bottom right plots in Figure 2. The functional dependence on Mach the Mach number,  $\exp(x_{cr}) \propto \mathcal{M}^2$ , is the same for all KM and PN models. However, both the KM and KM-FK models lack a free-fall weighing factor in the integrand:  $f_{ff} = 1$ , independent of  $x_{cr}$  (see second column in table 1). For this reason,  $\epsilon_{mod}$  rapidly drops with increasing  $K_{SGS} \propto \mathcal{M}^2$ , which strongly suppresses star formation as soon as stellar feedback kicks in (about 4 Myr after creation of the first stars). The suppressed star formation in turn prevents feedback from becoming sufficiently strong to expand and destroy a region with active/recent star formation. This results gradually growing global star formation rates in the KM and KM-FK simulations, without reaching statistically stable disk configurations.

### 3.2.4 PHN-model

In contrast to the analytical models, PHN assume a strong increase of  $\epsilon_{mod}$  with the cold-phase density through the exponential dependence on the virial parameter. This avoids a continuously drifting star formation rate such as in the KM simulation. Nonetheless, the level of  $\epsilon_{mod}$  following from the PHN model is systematically too low in the regime that is relevant for star formation. As shown in Section 3.3, this results in a extremely clumpy disk, which only slowly reaches a stable configuration. Although the fit formula for  $\epsilon_{mod}$  put forward by PHN<sup>5</sup> depends only on the virial parameter  $\alpha_{vir} \propto K_{SGS}$ , the lower envelope of the  $\epsilon_{mod}$ - $K_{SGS}$ -distribution shown in Fig. 2 suggests a quadratic dependence on  $K_{SGS}$ . This non-linear behaviour is a consequence of the implicit  $K_{SGS}$ -dependencies of the cold-gas density  $\rho_{c,pa}$  and the clump scale  $\ell_c$ .

## 3.3 Disk structure and probability density functions

By comparing the gaseous disk structure for the different runs in Fig. 3, it can be seen that deviations of the star formation rate caused by different average levels of  $\epsilon_{mod}$  go along with changes in the disk structure. This is obvious for the cases KM, KM-FK, and PHN, which produce much clumpier disks. To a lesser degree, also the disk in the PN run tends to be clumpier as compared to PN-FK. Virtually no differences can be seen for the runs from the HC-family, which also compare well to PN-FK. In extreme cases (KM and PHN), the disks are dominated by the presence of very massive, and dense clumps ( $\Sigma \gtrsim 10^3 \text{ M}_\odot \text{ pc}^{-2}$ ). The void areas ( $\Sigma \ll 1 \text{ M}_\odot \text{ pc}^{-2}$ ) between these clumps are only intercepted by tidal tails and bridges that form during mergers and fly-by interactions of clusters. As a result, a similar star formation rate such as in the late stages of the PHN and PN-FK runs does not necessarily imply similar disk structures.

In the KM and PHN runs, we find extremely massive clumps with very high column densities ( $\Sigma \gtrsim 10^3 \text{ M}_\odot \text{ pc}^{-2}$ ). This is in stark contrast to other runs (PN-FK, PN-FK-mff, HC family, and KM-FK-mff), where gas of moderate density

( $1 \text{ M}_\odot \text{ pc}^{-2} \lesssim \Sigma \lesssim 100 \text{ M}_\odot \text{ pc}^{-2}$ ) is concentrated in spiral-like structures with substantially smaller clumps, similar to the initial disk at at 1 Gyr. Denser, star forming regions are eventually disrupted by the violent expansion induced by SN feedback, but the low-density gas is less space filling in these runs. The disks in the PN and the KM-FK runs are intermediate cases.

A more accurate distinction is possible by means of probability density functions of the gas column density weighted by by area or by the mass fraction  $\Sigma_X/\Sigma$ , where  $\Sigma_X$  either stands for the column density of cold gas,  $\Sigma_c$ , or the column density of shielded molecular gas,  $\Sigma_{H_2}$ . The results for the different simulation runs are shown in Fig. 4. The normalisations of  $\text{pdf}[\log_{10}(\Sigma)]$  and  $\text{pdf}_{\Sigma_X/\Sigma}[\log_{10}(\Sigma)]$  are, respectively, given by

$$\int_{-\infty}^{\infty} \text{pdf}[\log_{10}(\Sigma)] d[\log_{10}(\Sigma)] = 1 \quad (14)$$

and

$$\int_{-\infty}^{\infty} \text{pdf}_{\Sigma_X/\Sigma}[\log_{10}(\Sigma)] d[\log_{10}(\Sigma)] = \frac{M_X}{M}. \quad (15)$$

One can distinguish at least four different regimes in the plot of  $\text{pdf}[\log_{10}(\Sigma)]$  in the upper left panel of Fig. 4:

(i)  $\Sigma \lesssim 2 \times 10^{-1} \text{ M}_\odot \text{ pc}^{-2}$ : Gas found in this range is extremely hot and dilute and was most likely recently produced by SNe.

(ii)  $2 \times 10^{-1} \text{ M}_\odot \text{ pc}^{-2} \lesssim \Sigma \lesssim 3 \times 10^0 \text{ M}_\odot \text{ pc}^{-2}$ : In this range and also at higher densities, there is an approximate balance between heating and radiative cooling. The two prominent maxima of the pdfs correspond to the collisional ionisation of hydrogen at  $\approx 2 \times 10^0 \text{ M}_\odot \text{ pc}^{-2}$  and helium at  $\approx 5 \times 10^{-1} \text{ M}_\odot \text{ pc}^{-2}$ , respectively. For this reason, there is hardly any gas in the cold phase below a density of  $\approx 2 \times 10^0 \text{ M}_\odot \text{ pc}^{-2}$  (compare top and middle plots in Fig. 4).

(iii)  $3 \times 10^0 \text{ M}_\odot \text{ pc}^{-2} \lesssim \Sigma \lesssim 10^2 \text{ M}_\odot \text{ pc}^{-2}$ : In this regime, the cold and warm phases coexist. The distribution of the cold gas shown in the middle plot in Fig. 4 has an approximately log-normal shape, with a maximum at  $\Sigma \approx 2 \times 10^1 \text{ M}_\odot \text{ pc}^{-2}$ . The existence of a cold phase can also be seen as a hump in  $\text{pdf}[\log_{10}(\Sigma)]$ . Above densities of about  $\approx 1 \times 10^1 \text{ M}_\odot \text{ pc}^{-2}$ , shielded molecular gas may be present inside of the cold phase (see bottom plot).

(iv)  $\Sigma \gtrsim 10^2 \text{ M}_\odot \text{ pc}^{-2}$ : Due to significant gravitational self-interactions of gas and stars, both  $\text{pdf}[\log_{10}(\Sigma)]$  and  $\text{pdf}_{\Sigma_c/\Sigma}[\log_{10}(\Sigma)]$  show an excess in their high density tails. The gas in this regime resides in the prominent, more or less gravitationally bound knots and clumps that are visible in Fig. 3. Shielded molecular gas makes up the major fraction of the cold phase, but there is also gas in the warm phase because of the evaporation of cold gas due to SN feedback.

Differences induced by the star formation models are most evident in the density regime (iv), in which most of the star formation happens. There is an enormous excess of high-density gas in case of PHN and KM. The maxima of shielded molecular gas are found at roughly ten times higher  $\Sigma$  ( $\approx 6 \times 10^1 \text{ M}_\odot \text{ pc}^{-2}$ ) compared to the maxima in the other runs. The lack of intermediate density gas as well as the increased abundance of low-density gas in PHN and KM is readily visible in the regimes (iii) and (iv). The pdfs from the KM-FK and the PN run exhibit significantly less

<sup>5</sup> This formula is not based on any physical ideas. It is merely a fit to the data points obtained from their simulation suite.

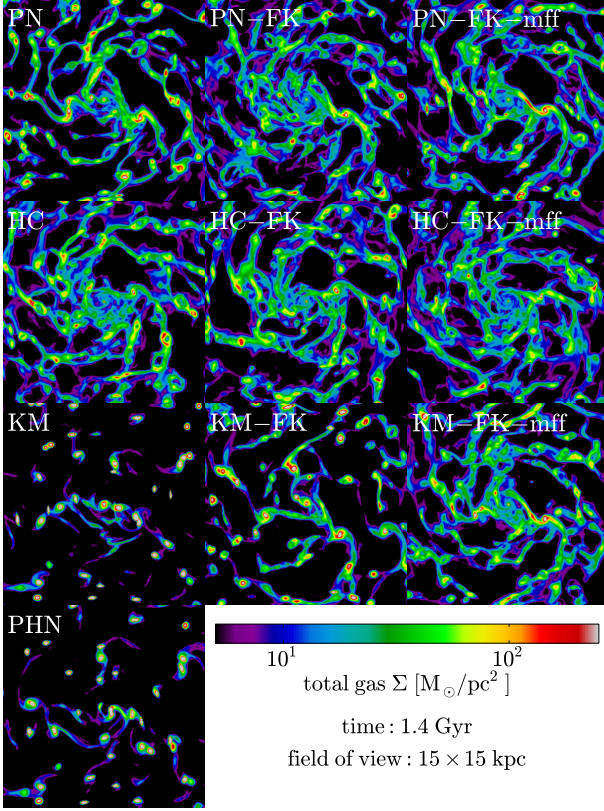


**Figure 3.** Projections of the total gas density  $\rho$  perpendicular to the disk plane in an area of  $15 \times 15$  kpc around the galactic centre. The individual projections depict the state of the disk in the indicated run at  $\sim 1.4$  Gyr.

pronounced high-density tails, but they are still stronger than the tails obtained with the HC-family, PN-FK, PN-FK-mff, and KM-FK-mff models.

Observationally almost log-normal shaped pdfs are found for gas in nearby galaxies (e.g. Berkhuijsen & Fletcher 2015; Hughes et al. 2013). The pdf of CO-line emitting gas in M51 by Hughes et al. (2013) is based on data of comparable spatial resolution (40 pc). Most of what we consider as cold phase gas ( $\Sigma_c$ ) would be seen in such observations, but a significant fraction of it is actually atomic, particularly for lower  $\Sigma$ . Compared to observed pdfs (e.g. Figure 2a in Hughes et al. 2013), the maximum of  $\text{pdf}_{\Sigma_c/\Sigma}[\log_{10}(\Sigma)]$  computed from our simulations is thus shifted toward lower densities. Apart from that, M51 is an interacting galaxy in which highly compressed gas is expected to be more abundant than in an isolated, quiescent galaxy. Nevertheless, the general shape and especially the high-density tail as inferred from the HC-family, PN-FK, PN-FK-mff, and KM-FK-mff model runs are consistent with the observations of Hughes et al. (2013), while PHN and KM are clearly ruled out.

A comparison with the simulations of Hopkins et al. (2012) shows pdfs that are populated up to much higher densities. This appears to be a consequence of the significantly higher numerical resolution, but also the star formation recipe used in their simulations. Specifically, the low efficiency and the rather high star formation threshold favour the formation of denser clouds and a higher global star formation rate (cf. their ‘Sbc’-runs).

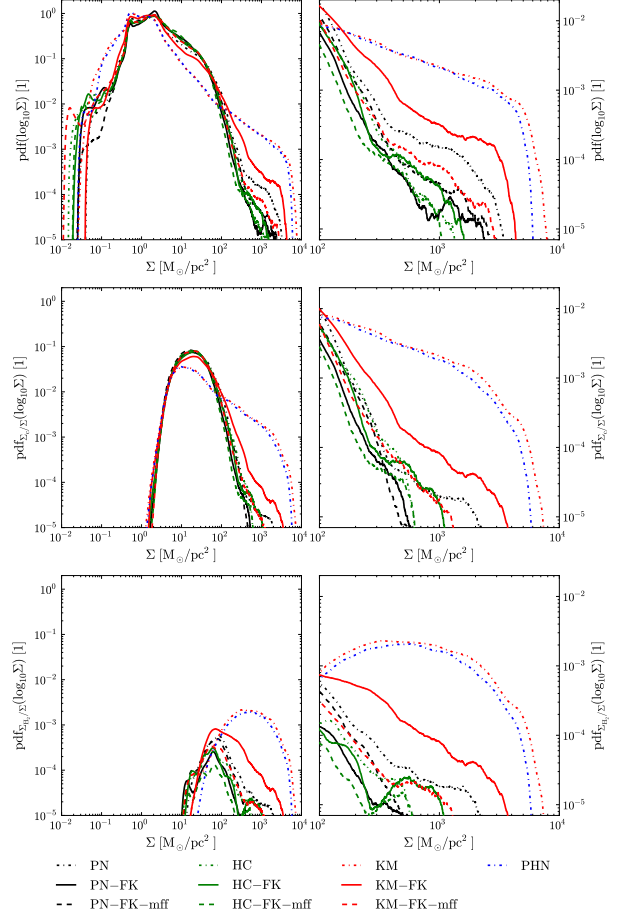


**Figure 4.** **Top left:** Area weighted probability density function  $\text{pdf}(\log_{10} \Sigma)$  of the logarithmic total gas column density in the disks versus total gas column density  $\Sigma$  for all runs at a simulated age of  $\sim 1.4$  Ga. Arrangement of line colours and styles like in Fig. 1. **Top right:** Detail of the plot on the left for  $\Sigma > 10^2$   $M_{\odot} \text{pc}^{-3}$ . **Middle left:** Probability density function  $\text{pdf}_{\Sigma_c/\Sigma}(\log_{10} \Sigma)$  weighted by the cold phase gas fraction  $\Sigma_c/\Sigma$  versus  $\Sigma$ . **Middle right:** Detail of the plot on the left for  $\Sigma > 10^2$   $M_{\odot} \text{pc}^{-3}$ . **Bottom left:** Probability density function  $\text{pdf}_{\Sigma_{\text{H}_2}/\Sigma}(\log_{10} \Sigma)$  weighted by the shielded molecular gas fraction  $\Sigma_{\text{H}_2}/\Sigma$  versus  $\Sigma$ . **Bottom right:** Detail of the plot on the left for  $\Sigma > 10^2$   $M_{\odot} \text{pc}^{-3}$ .

### 3.4 Star formation relations

With the exception of the KM and PHN runs, a robust relation between the star-formation column density  $\dot{\Sigma}_{\text{SF}}$  and column density of shielded, molecular gas is established (see Fig. 5). However, the inferred time scales  $\tau_{\text{SF,H}_2}$  of star formation in molecular gas vary between  $\approx 80$  Myr and  $\approx 0.5$  Gyr. As pointed out in BS14, time scales around  $\approx 100$  Myr are reasonable because the simplified model for the molecular fraction  $f_{\text{H}_2}$  in our simulations is biased toward high-density, star-forming regions. Observational analogues of what is treated as shielded molecular gas in our simulations favour short star formation time scales  $\sim 100$  Myr (e.g. Gao & Solomon 2004; Evans et al. 2009; Murray 2011). Keeping that in mind, the star formation rate is anomalously low for a wide range of  $\Sigma_{\text{H}_2}$  column densities for the KM- and the PHN-model, with a very sharp rise at

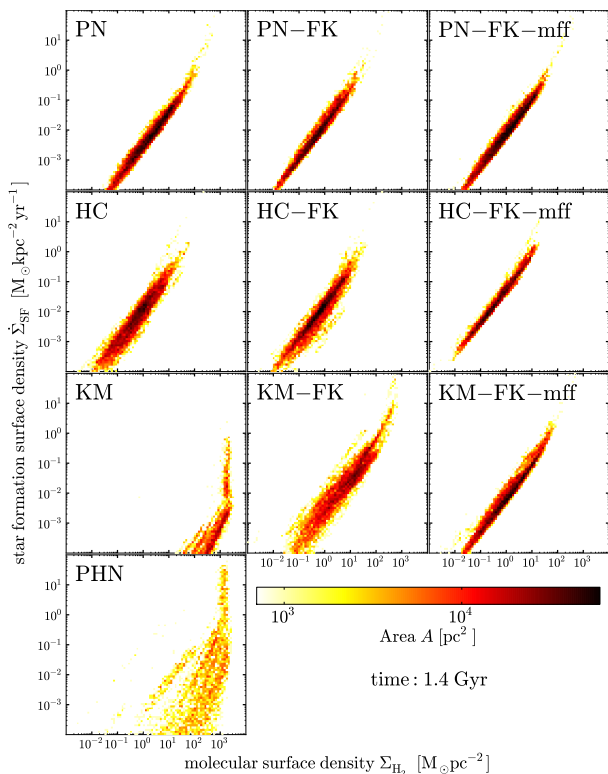


**Figure 5.** Comparison of area-weighted 2D histograms of the star formation column density  $\dot{\Sigma}_s$  vs. the column density  $\Sigma_{\text{H}_2}$  of shielded, molecular gas at an age of  $\sim 1.4$  Gyr. The area is logarithmically colour-coded.

$\Sigma_{\text{H}_2} \sim 10^3 \text{ M}_\odot \text{pc}^{-2}$ . Moreover the spread is significantly larger in these cases. Such a  $\dot{\Sigma}_{\text{SF}}\text{-}\Sigma_{\text{H}_2}$ -relation is definitely not consistent with their observational counterparts. For the KM-FK and PN models, the relations are slightly tilted upwards at the high-density end.<sup>6</sup> Basically, the results show that star formation is shifted to much higher molecular column densities for the models in the KM family, particularly for the original KM model, and also for the PHN model. Generally, the multi free-fall models produce tighter correlations between  $\dot{\Sigma}_{\text{SF}}$  and  $\Sigma_{\text{H}_2}$ . The tightest correlation is found for HC-FK-mff, with a particularly short star formation time scale.

The 2D histograms of  $\dot{\Sigma}_{\text{SF}}$  vs.  $\Sigma$  (total gas column density) in Fig. 6 show qualitatively the same behaviour as described in BS14. Star formation is cut off below  $\Sigma \approx 10^0 \text{ M}_\odot \text{pc}^{-2}$  because of the lack of shielded, molecular gas. Above this threshold,  $\dot{\Sigma}_{\text{SF}}$  steeply rises and then gradually flattens to an approximate KS-relation  $\dot{\Sigma}_{\text{SF}} \propto \Sigma_{\text{KS}}^{\alpha_{\text{KS}}}$  with  $\alpha_{\text{KS}} \approx 2$ . The exponent  $\alpha_{\text{KS}} \approx 2$  is indicative of star bursts.

<sup>6</sup> This is actually a consequence of a lower bound for the cold-gas fraction at densities above  $500 \text{ cm}^{-3}$ . For the fiducial model, this was intended to prevent star formation from being completely quenched by feedback in very dense regions, which hardly affected the  $\dot{\Sigma}_{\text{SF}}\text{-}\Sigma_{\text{H}_2}$ -relation (see for example, the PN-FK panel in Fig. 5). For extremely clumpy disks, the star formation rate is artificially pushed upwards. We did not adjust the threshold density for the cold-gas floor when carrying out our comparison study.

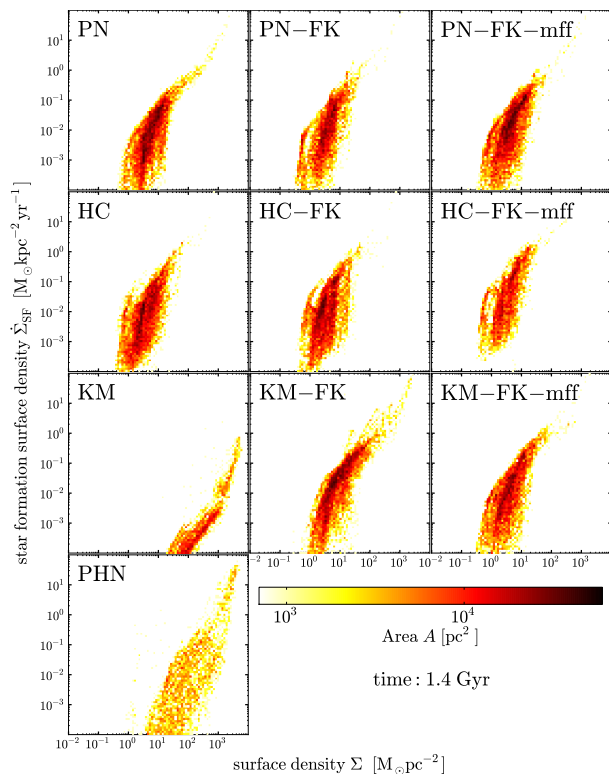


**Figure 6.** 2D histograms as in Fig. 5 for the star formation column density  $\dot{\Sigma}_s$  vs. the total gas column density  $\Sigma$ .

This is plausible, since the simulated galaxies are still gas-dominated after 1.4 Gyr. Again, the star formation obtained with the KM, KM-FK, and PHN models deviates more or less from the other cases.

## 4 DISCUSSION AND CONCLUSIONS

In this paper we presented results of a suite of ten isolated disk galaxy simulations carried out using the cosmological hydrodynamics code *Nyx* (Almgren et al. 2013), featuring a turbulence SGS model (Schmidt & Federrath 2011; Schmidt et al. 2014) and the MIST model (BS12; BS14) for the turbulent multi-phase ISM. In each of the runs, a different analytic star-formation model from the literature was applied (FK12; HC08-13; KM05; PN11; PHN12, see Table 1 for the analytical expressions employed here). These models for the sub-resolution structure of the ISM were incorporated into the MIST framework to estimate the local star formation efficiency  $\epsilon_{\text{mod}}$  in the cold molecular gas. We used an evolved (for 1 Gyr) disk from the 'ref' run of BS14, which resembles a gas-rich, quiescent star forming spiral galaxy, as initial condition to start the runs with different star formation models. This approach minimised effects caused by the rapid growth of stellar mass and metallicity during the initial transient. From this initial condition every simulation was evolved over additional 0.4 Gyr, which allows the star forming disk to settle into a new equilibrium in most cases. Several important properties resulting from the local self-regulation in MIST, as reported by BS14, are recovered in our simulation runs independent of the choice of the star formation efficiency  $\epsilon_{\text{mod}}$  if the KM, KM-FK, and PHN models are excluded:

- A global star formation rate around  $\dot{M}_{\text{SF}} \approx 2.5 M_{\odot} \text{yr}^{-1}$  is maintained. This is a typical value for a quiescent isolated spiral galaxy.

- Model-dependent variations of  $\epsilon_{\text{mod}}$  do not significantly affect the amount of shielded molecular gas. As a result, the almost linear relationship between local star formation rate column density  $\dot{\Sigma}_{\text{s}}$  and column density  $\Sigma_{\text{H}_2}$  of shielded molecular gas turns out to be very robust in the framework of MIST. However, the inferred depletion time scales vary between 80 Myr and 0.5 Gyr, depending on the star formation model. With respect to observational findings, a depletion time scale  $< 100$  Myr is more plausible (Gao & Solomon 2004; Murray 2011). Moreover, a tighter correlation is obtained for the multi free-fall models.

- Our star forming regions have a typical life-cycle of 10...30 Myr. A fraction of  $\sim 10$  per cent of their gaseous mass is converted into stars during that period, which matches observational estimates (e.g. Blitz et al. 2007; McKee & Ostriker 2007; Miura et al. 2012) as well as simulation results by e.g. Hopkins et al. (2012) and Tasker et al. (2015). We also find long-lived giant star forming clumps similar to those described by Bournaud et al. (2014) in our simulations.

- Cold-gas density pdfs are comparable to observational counterparts (see, for example, Hughes et al. 2013), particularly at the high densities that are required for star formation.

- The high-density tails of our  $\dot{\Sigma}_{\text{s}}-\Sigma$ -distributions suggest a KS-relationship  $\dot{\Sigma}_{\text{s}} \propto \Sigma^{\alpha_{\Sigma}}$  with  $\alpha_{\Sigma} \approx 2$ , which is expected for environments dominated by gas dynamics.

- Star formation mainly occurs in the SGS turbulence energy range  $10 \text{ km}^2 \text{s}^{-2} \lesssim K_{\text{SGS}} \lesssim 10^3 \text{ km}^2 \text{s}^{-2}$ , with a peak around  $10^2 \text{ km}^2 \text{s}^{-2}$ . This value corresponds to a 3D-velocity dispersion in the range  $\sigma_{\text{u}} \approx 3 \text{ km s}^{-1} \dots 30 \text{ km s}^{-1}$ , which is in good agreement with observations of star forming regions (e.g. Leroy et al. 2008; Shetty et al. 2012; Stilp et al. 2013) (since these regions are more or less unresolved in our simulations, the SGS turbulence energy  $K_{\text{SGS}}$  is the relevant quantity). A minimum level of turbulence is necessary to boost the molecular hydrogen formation rates. On the other hand, there is an upper bound on  $K_{\text{SGS}}$  because high values of  $K_{\text{SGS}}$  are produced by intense stellar feedback, which tend to disrupt star forming regions. This effect also limits the duty cycle of star forming regions to around 10...30 Myr in our simulation runs, in agreement with observational estimates (e.g. Blitz et al. 2007; McKee & Ostriker 2007; Miura et al. 2012).

For most models,  $\epsilon_{\text{mod}}$  is effectively a function of  $K_{\text{SGS}}$ . The scatter of  $\epsilon_{\text{mod}}$  in Fig. 2 indicates a subdominant dependency on other quantities such as the density, for example, in the case of PHN. For  $\epsilon_{\text{mod}} \sim 0.1$ , corresponding to molecular gas depletion time scales of  $\lesssim 100$  Myr in the simulations, the gaseous star forming disks are moderately clumpy and exhibit pronounced transient spiral-like, flocculent features connecting knots and clumps. If  $\epsilon_{\text{mod}}$  is substantially lower in the interval of turbulence energy values that admit significant star formation, the disk structure changes. This particularly happens with the KM, KM-FK, and PHN models, which produce either too many or not enough stars to support the initial disk configuration through feedback. In these runs, the disk undergoes a transition to a different configuration with markedly more massive and compact clumps

accompanied by tidal tails and bridges. Such extremely massive clumps appear to be common in star forming, gas-rich galaxies at high redshifts  $\sim 2$  (e.g. Zanella et al. 2015; Guo et al. 2012). Similar structures are found in some simulations of gas-rich galaxies (e.g. by Hopkins et al. 2011; Bournaud et al. 2014). However, the models considered here are intended to describe conditions in fairly regular star forming regions, which are found in almost bulge-less and gas-rich spiral galaxies without any external disturber. Some of the models clearly fail to produce a disk structure that even remotely resemble such galaxies. However, the strong negative coupling between star formation efficiency and turbulence produced by stellar feedback, for example, in the case of the KM model, might help to gain a better understanding of galaxies dominated by massive clumps. Which factors actually select the mode of star formation is left as an open question.

If additional feedback processes like winds from young, massive stars were incorporated in our simulations, the global star formation rate would be shifted, but the self-regulation mechanism would basically remain intact. Apart from that, the star formation rate would be altered if the circumgalactic medium were properly taken into account (such as in cosmological zoom-in simulations). This has to be investigated in future studies.

Both KM and KM-FK do not feature a free-fall time factor (i.e.  $f_{\text{ff}} = 1$ , meaning that the effective free-fall time scale is given by the mean density of the gas in cold phase), while all other theoretical models use some weighing factor to modify the effective free-fall time scale. In our simulations, this turns out to be an essential feature to reproduce observed properties of nearby disk galaxies and their star forming regions. The importance of a non-trivial free-fall factor, such as in the PN and the HC models, was also highlighted by FK12. Moreover, we can confirm that the calibrations established by this study generally result in improvements. Although FK12 found higher residual  $\chi^2$ -values for the best-fit HC models than for the competing models, our simulations suggest that the models from the HC family yield the most plausible results in terms of the correlation between star formation rate and molecular hydrogen column density, the cold-gas pdf, and the disk structure. However, the differences compared to the PN-FK and PN-FK-mff runs are really minor. Also the KM model produces consistent results if it is applied in the multi free-fall formulation with the new calibration of FK12.

In contrast to all other models in our suite, the star formation efficiency in the simple PHN model has no functional dependence on the Mach number and, consequently, is ignorant of the fundamentally different nature of subsonic and supersonic turbulent fluctuations. This does not appear plausible, because the width of the density pdf is basically determined by the turbulent Mach-number in the cold phase  $\mathcal{M}$  (see equation 6). However, PHN12 incorporate magnetic fields, which might also influence the star formation efficiency, although probably to a lesser degree. Possibly, the model could be improved by establishing a fit function from turbulence simulations covering a larger parameter space, e.g. by including non-solenoidal forcing.

A further distinction between the models that are so far consistent with the observational requirements – namely, PN-FK, PN-FK-mff, HC, HC-FK, HC-FK-mff, and

KM-FK-mff – might be possible on the basis of observational measurements of the turbulent velocity dispersion on molecular-cloud scales and associated star formation efficiencies. On the theoretical side, constraints on the relation between star formation efficiency and parameters related to turbulence can be obtained from high-resolution simulations of star forming clouds such as in the seminal work by FK12. However, any such simulations make idealised assumptions about initial and boundary conditions for molecular-cloud turbulence. To check the consistency of models for the dynamical star formation efficiency, it will be necessary to re-simulate a star-forming region in global disk galaxy simulation such that star formation processes are fully resolved and then to compare the results with the assumptions that went into the model.

## ACKNOWLEDGEMENTS

We thank Peter Nugent and his team for supporting the development of *Nyx* at the Computational Cosmology Center at LBNL. In particular, we thank Ann Almgren for her help with the implementation of the code components used in this work. We also thank Jens Niemeyer for discussions and comments and we are grateful for valuable comments by the anonymous referee that helped us to improve this paper. H. Braun was financially supported by the CRC 963 of the German Research Council. The simulations presented in this article were performed on SuperMUC of the LRZ (project pr47bi) in Germany. We also acknowledge the yt toolkit by Turk et al. (2011) that was used for our analysis of numerical data.

## References

- Agertz O., Kravtsov A. V., 2014, ArXiv e-prints, 1404.2613  
 Agertz O., Kravtsov A. V., Leitner S. N., Gnedin N. Y., 2013, *ApJ*, 770, 25  
 Almgren A. S., Bell J. B., Lijewski M. J., Lukić Z., Van Andel E., 2013, *ApJ*, 765, 39  
 Berkhuijsen E. M., Fletcher A., 2015, *MNRAS*, 448, 2469  
 Bigiel F., Leroy A. K., Walter F., Brinks E., de Blok W. J. G., Kramer C., Rix H. W., Schrubba A., Schuster K.-F., Usero A., Wiesemeyer H. W., 2011, *ApJ*, 730, L13+  
 Blitz L., Fukui Y., Kawamura A., Leroy A., Mizuno N., Rosolowsky E., 2007, *Protostars and Planets V*, pp 81–96  
 Bournaud F., Perret V., Renaud F., Dekel A., Elmegreen B. G., Elmegreen D. M., Teyssier R., Amram P., Daddi E., Duc P.-A., Elbaz D., Epinat B., Gabor J. M., Juneau S., Kraljic K., Le Floch E., 2014, *ApJ*, 780, 57  
 Braun H., Schmidt W., 2012, *MNRAS*, 421, 1838  
 Braun H., Schmidt W., Niemeyer J. C., Almgren A. S., 2014, *MNRAS*, 442, 3407  
 Daddi E., Bournaud F., Walter F., Dannerbauer H., Carilli C. L., Dickinson M., Elbaz D., Morrison G. E., Riechers D., Onodera M., Salmi F., Krips M., Stern D., 2010, *ApJ*, 713, 686  
 Dobbs C. L., Pringle J. E., 2013, *MNRAS*, 432, 653  
 Evans II N. J., Dunham M. M., Jørgensen J. K., Enoch M. L., Merín B., van Dishoeck E. F., coauthors ., 2009, *ApJS*, 181, 321  
 Federrath C., Klessen R. S., 2012, *ApJ*, 761, 156  
 Federrath C., Roman-Duval J., Klessen R. S., Schmidt W., Mac Low M., 2010, *A&A*, 512, A81+  
 Gao Y., Solomon P. M., 2004, *ApJ*, 606, 271  
 Genzel R., Tacconi L. J., Gracia-Carpio J., Sternberg A., Cooper M. C., Shapiro K., co authors ., 2010, *MNRAS*, 407, 2091  
 Gnedin N. Y., Tassis K., Kravtsov A. V., 2009, *ApJ*, 697, 55  
 Guo Y., Gialvalisco M., Ferguson H. C., Cassata P., Koekoemoer A. M., 2012, *ApJ*, 757, 120  
 Hennebelle P., Chabrier G., 2008, *ApJ*, 684, 395  
 Hennebelle P., Chabrier G., 2009, *ApJ*, 702, 1428  
 Hennebelle P., Chabrier G., 2011, *ApJ*, 743, L29  
 Hennebelle P., Chabrier G., 2013, *ApJ*, 770, 150  
 Hennebelle P., Falgarone E., 2012, *A&A Rev.*, 20, 55  
 Hopkins P. F., Kereš D., Oñorbe J., Faucher-Giguère C.-A., Quataert E., Murray N., Bullock J. S., 2014, *MNRAS*, 445, 581  
 Hopkins P. F., Quataert E., Murray N., 2011, *MNRAS*, 417, 950  
 Hopkins P. F., Quataert E., Murray N., 2012, *MNRAS*, 421, 3488  
 Hughes A., Meidt S. E., Schinnerer E., Colombo D., Pety J., Leroy A. K., Dobbs C. L., García-Burillo S., Thompson T. A., Dumas G., Schuster K. F., Kramer C., 2013, *ApJ*, 779, 44  
 Kennicutt R. C., Evans N. J., 2012, *ARA&A*, 50, 531  
 Kennicutt Jr. R. C., 1998, *ApJ*, 498, 541  
 Krumholz M. R., McKee C. F., 2005, *ApJ*, 630, 250  
 Lada C. J., Lombardi M., Alves J. F., 2010, *ApJ*, 724, 687  
 Lagos C. d. P., Crain R. A., Schaye J., Furlong M., Frenk C. S., Bower R. G., Schaller M., Theuns T., Trayford J. W., Bahe Y. M., Dalla Vecchia C., 2015, *ArXiv e-prints*, 1503.04807  
 Leroy A. K., Walter F., Brinks E., Bigiel F., de Blok W. J. G., Madore B., Thornley M. D., 2008, *AJ*, 136, 2782  
 Mac Low M.-M., Klessen R. S., 2004, *Reviews of Modern Physics*, 76, 125  
 McKee C. F., Ostriker E. C., 2007, *ARA&A*, 45, 565  
 Miura R. E., Kohno K., Tosaki T., Espada D., Hwang N., Kuno N., coauthors ., 2012, *ApJ*, 761, 37  
 Murray N., 2011, *ApJ*, 729, 133  
 Onodera S., Kuno N., Tosaki T., Kohno K., Nakanishi K., Sawada T., Muraoka K., Komugi S., Miura R., Kaneko H., Hirota A., Kawabe R., 2010, *ApJ*, 722, L127  
 Padoan P., Haugbølle T., Nordlund Å., 2012, *ApJ*, 759, L27  
 Padoan P., Nordlund Å., 2011, *ApJ*, 730, 40  
 Renaud F., Bournaud F., Emsellem E., Elmegreen B., Teyssier R., Alves J., Chapon D., Combes F., Dekel A., Gabor J., Hennebelle P., Kraljic K., 2013, *MNRAS*  
 Roychowdhury S., Huang M.-L., Kauffmann G., Wang J., Chengalur J. N., 2015, *MNRAS*, 449, 3700  
 Schmidt M., 1959, *ApJ*, 129, 243  
 Schmidt W., Almgren A. S., Braun H., Engels J. F., Niemeyer J. C., Schulz J., Mekuria R. R., Aspden A. J., Bell J. B., 2014, *MNRAS*, 440, 3051  
 Schmidt W., Collins D. C., Kritsuk A. G., 2013, *MNRAS*, 431, 3196  
 Schmidt W., Federrath C., 2011, *A&A*, 528, A106+  
 Schrubba A., 2013, in Wong T., Ott J., eds, *IAU Symposium*

- Vol. 292 of IAU Symposium, The Star Formation Relation in Nearby Galaxies. pp 311–318
- Shetty R., Beaumont C. N., Burton M. G., Kelly B. C., Klessen R. S., 2012, *MNRAS*, 425, 720
- Stilp A. M., Dalcanton J. J., Warren S. R., Weisz D. R., Skillman E., Ott J., Williams B. F., Dolphin A. E., 2013, *ApJ*, 772, 124
- Stinson G., Seth A., Katz N., Wadsley J., Governato F., Quinn T., 2006, *MNRAS*, 373, 1074
- Stinson G. S., Brook C., Macciò A. V., Wadsley J., Quinn T. R., Couchman H. M. P., 2013, *MNRAS*, 428, 129
- Tasker E. J., Wadsley J., Pudritz R., 2015, *ApJ*, 801, 33
- Turk M. J., Smith B. D., Oishi J. S., Skory S., Skillman S. W., Abel T., Norman M. L., 2011, *ApJS*, 192, 9
- Wang H.-H., Klessen R. S., Dullemond C. P., van den Bosch F. C., Fuchs B., 2010, *MNRAS*, 407, 705
- Wise J. H., Abel T., Turk M. J., Norman M. L., Smith B. D., 2012, *MNRAS*, 427, 311
- Zanella A., Daddi E., Le Floc’h E., Bournaud F., Gobat R., Valentino F., Strazzullo V., Cibinel A., Onodera M., Perret V., Renaud F., Vignali C., 2015, *Nature*, 521, 54

This paper has been typeset from a  $\text{\TeX}/\text{\LaTeX}$  file prepared by the author.